

# NO<sub>x</sub> Reduction over Smart Catalysts with Self-Created Targeted Antipoisoning Sites

Jialun Zhou, Penglu Wang, Aling Chen, Wenqiang Qu, Yufei Zhao, and Dengsong Zhang\*



Cite This: *Environ. Sci. Technol.* 2022, 56, 6668–6677



Read Online

ACCESS |



Metrics & More



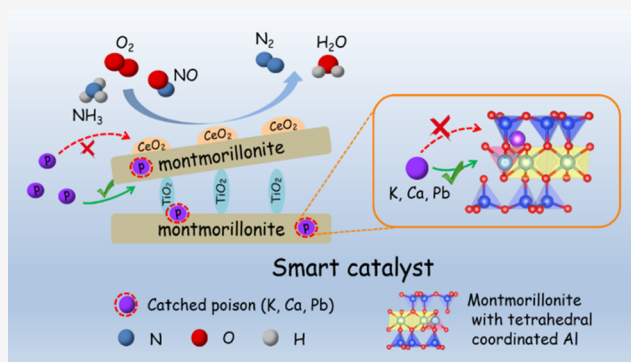
Article Recommendations



Supporting Information

**ABSTRACT:** Selective catalytic reduction of NO<sub>x</sub> in the presence of alkali (earth) metals and heavy metals is still a challenge due to the easy deactivation of catalysts. Herein, NO<sub>x</sub> reduction over smart catalysts with self-created targeted antipoisoning sites is originally demonstrated. The smart catalyst consisted of TiO<sub>2</sub> pillared montmorillonite with abundant cation exchange sites to anchor poisoning substances and active components to catalyze NO<sub>x</sub> into N<sub>2</sub>. It was not deactivated during the NO<sub>x</sub> reduction process in the presence of alkali (earth) metals and heavy metals. The enhanced surface acidity, reducible active species, and active chemisorbed oxygen species of the smart catalyst accounted for the remarkable NO<sub>x</sub> reduction efficiency. More importantly, the self-created targeted antipoisoning sites expressed specific anchoring effects on poisoning substances and protected the active components from poisoning. It was demonstrated that the tetrahedrally coordinated aluminum species of the smart catalyst mainly acted as self-created targeted antipoisoning sites to stabilize the poisoning substances into the interlayers of montmorillonite. This work paves a new way for efficient reduction of NO<sub>x</sub> from the complex flue gas in practical applications.

**KEYWORDS:** air pollution control, environmental catalysis, NO<sub>x</sub> removal, selective catalytic reduction, poisoning resistance, smart catalysts



## 1. INTRODUCTION

Nitrogen oxides emitted from the fuel-fired flue gas are extremely harmful to human health and ecosystems.<sup>1,2</sup> Among various air pollutant control technologies, selective catalytic reduction (SCR) of NO<sub>x</sub> into N<sub>2</sub> has been demonstrated to be the most effective way to reduce NO<sub>x</sub> emissions in stationary sources.<sup>3,4</sup> The commercial V<sub>2</sub>O<sub>5</sub>-WO<sub>3</sub>(MoO<sub>3</sub>)/TiO<sub>2</sub> catalyst has been widely applied in NO<sub>x</sub> reduction from the complex flue gas.<sup>5</sup> However, the current catalysts are easily deactivated by alkali (earth) metals and heavy metals in the flue gas.<sup>6</sup> Even the widely studied cerium-based catalysts with excellent NO<sub>x</sub> reduction efficiency are still plagued by poisoning metals.<sup>7–9</sup> Therefore, it is urgent to exploit highly efficient antipoisoning catalysts.

Generally, the alkali (earth) metals and heavy metals will occupy the acid and redox sites to restrain the NH<sub>3</sub> and NO<sub>x</sub> adsorption and activation over SCR catalysts.<sup>10–12</sup> Meanwhile, metal oxides formed by alkali (earth) metals and heavy metals will also block the channels, which severely affects the diffusion of reactants.<sup>12–14</sup> The strategies reported for promoting the resistance to alkali (earth) metals and heavy metals include the introduction of excess acidic sites, the utilization of strongly acidic carriers, the application of special structures, the construction of poisoning capture sites, etc.<sup>15</sup> Previously, we

constructed SO<sub>4</sub><sup>2–</sup> on the V<sub>2</sub>O<sub>5</sub>-S/CeO<sub>2</sub> catalyst as sacrifice sites, making K bind to SO<sub>4</sub><sup>2–</sup> in the first place to protect the active component V = O species, which greatly improved the alkali metal resistance.<sup>16</sup> In addition, Jing et al.<sup>17</sup> built a MoO<sub>3</sub> buffer layer between Fe<sub>2</sub>O<sub>3</sub> and TiO<sub>2</sub> carriers to capture sodium (Na) cations because the interaction between Na<sup>+</sup> and MoO<sub>3</sub> was stronger than that between Na<sup>+</sup> and Fe<sub>2</sub>O<sub>3</sub> and TiO<sub>2</sub>. In terms of alkali-earth metal and heavy metal resistance, Liang et al.<sup>12</sup> synthesized a solid superacid FeSTi catalyst with excellent resistance of Ca and Pb. The SO<sub>4</sub><sup>2–</sup> ions on the FeSTi catalyst surface could capture Ca and Pb well to form CaSO<sub>4</sub> and PbSO<sub>4</sub>, so the catalytic activity of FeSTi catalysts was not greatly affected. Furthermore, Wang et al.<sup>18</sup> found using the CeO<sub>2</sub> nanotubes as the support made catalysts have better alkali metal K and heavy metal Pb resistance compared with the CeO<sub>2</sub> nanoparticles, which benefited from the separation of active sites and poisoning capture sites. Although

**Received:** January 29, 2022

**Revised:** April 12, 2022

**Accepted:** April 18, 2022

**Published:** May 2, 2022



various attempts have been made to solve the alkali (earth) metal and heavy metal poisoning issue for SCR catalysts, the continuous deactivation of catalysts under practical application still exists as the main obstacle to restrain the further application of most SCR catalysts.

Montmorillonite (MMT) is a layered silica-aluminate clay with two layers of silica-oxygen tetrahedra and a layer of aluminum-oxygen octahedra sandwiched between them, which owns plenty of advantages including low cost, regular structure, and high cation exchange capability, endowing MMT with certain ability to anchor alkali (earth) metal and heavy metal cations via an ion-exchange process.<sup>19–21</sup> Nevertheless, the direct application of MMT materials into the  $\text{NH}_3$ -SCR reaction is not satisfactory and further modification methods are required to make the utilization of MMT in releasing alkali (earth) metal and heavy metal poisoning more reliable. MMT pretreated with an acid solution is confirmed to possess abundant Brønsted acid sites and a large number of ion-exchange sites in the layers, which provides appropriate fixing sites for alkali (earth) metals and heavy metals via the ion-exchange process, thus expressing excellent potential for improving the resistance of  $\text{NH}_3$ -SCR catalysts to alkali (earth) metals and heavy metals. Our previous study proved that the copillaring modification of Fe and Ti over MMT catalysts could improve the dispersion of the active component, which accounted for the high SCR activity as well as resistance to alkali and heavy metals.<sup>22</sup> However, the specific promotional mechanism of MMT for the improvement of poisoning resistance was still not clearly clarified.

In this work,  $\text{NO}_x$  reduction over smart catalysts with self-created targeted antipoisoning sites has been originally demonstrated. The smart catalysts using  $\text{TiO}_2$  pillared montmorillonite as support acquire superior  $\text{NO}_x$  reduction in the presence of alkali (earth) metals and heavy metals. The negligible influence of poisoning substances on structure, surface acidity, redox property, and reaction mechanism was proved to be responsible for the excellent antipoisoning ability of the smart catalyst. Furthermore, the specific anchoring effect of the self-created targeted antipoisoning sites on poisoning substances was clearly revealed. Noticeably, it was evidenced that the self-created targeted antipoisoning sites in  $\text{TiO}_2$ -pillared MMT were intrinsic tetrahedral-coordinated Al sites and effective pillared  $\text{TiO}_2$  species, which protected the active compounds from poisoning. This work not only gives a low-cost and efficient strategy for designing smart catalysts with high poisoning resistance in  $\text{NH}_3$ -SCR but also paves a new way for efficient reduction of  $\text{NO}_x$  from the complex flue gas in practical applications.

## 2. EXPERIMENTAL SECTION

**2.1. Catalyst Preparation.** The fresh MMT catalysts were obtained by nitric acid treatment, followed by  $\text{TiO}_2$  pillaring and  $\text{CeO}_2$  loading. First, 1 g of raw MMT was acidified with 9 mL of nitric acid solution ( $3 \text{ mol}\cdot\text{L}^{-1}$ ) at  $90^\circ\text{C}$  for 4 h to obtain the acidified MMT, which was named MMT-H. After that, 13.75 mL of nitric acid solution ( $3 \text{ mol}\cdot\text{L}^{-1}$ ) was added dropwise to a certain amount of tetrabutyl titanate and stirred at room temperature for 12 h to obtain the suspension, named solution A. At the same time, 1 g of MMT-H was added to 100 mL of deionized water to absorb water for 12 h at room temperature, with the resulting suspension named solution B. Then, solution A was added to solution B and stirred at  $60^\circ\text{C}$  for 6 h. The acquired solid was washed, dried, and finally

calcined at  $400^\circ\text{C}$  for 4 h to get  $\text{TiO}_2$ -pillared MMT, which was named MMT- $x\text{Ti}$ , where  $x$  represents the molar amount of pillared Ti. After that,  $\text{CeO}_2$  was supported on the MMT- $x\text{Ti}$  by an initial wet impregnation method to obtain  $y\text{CeO}_2/\text{MMT-}x\text{Ti}$  with various amounts of  $\text{CeO}_2$  loading, where  $y$  represents the weight amount of  $\text{CeO}_2$  loaded. Afterward, the alkali metal (K)-, alkali-earth metal (Ca)-, and heavy metal (Pb)-poisoned catalysts denoted K- $y\text{CeO}_2/\text{MMT-}x\text{Ti}$ , Ca- $y\text{CeO}_2/\text{MMT-}x\text{Ti}$ , Pb- $y\text{CeO}_2/\text{MMT-}x\text{Ti}$  were prepared via a typical wet impregnation method with the mass ratios of  $\text{K}_2\text{O}$ ,  $\text{CaO}$ , and  $\text{PbO}$  fixed at 1, 1, and 3 wt %, respectively. The obtained fresh catalysts were added to the  $\text{KNO}_3$ ,  $\text{Ca}(\text{NO}_3)_2$ , and  $\text{Pb}(\text{NO}_3)_2$  aqueous solutions under vigorous stirring at room temperature for 30 min, respectively, and the mixture was dried via rotary evaporation. K-, Ca-, and Pb-poisoned samples were calcined in air at  $400^\circ\text{C}$  and labeled as K- $y\text{CeO}_2/\text{MMT-}x\text{Ti}$ , Ca- $y\text{CeO}_2/\text{MMT-}x\text{Ti}$ , and Pb- $y\text{CeO}_2/\text{MMT-}x\text{Ti}$ , respectively. Among them, the alkali metal-poisoned one was selected as a typical case to investigate the antipoisoning effects and also named p- $y\text{CeO}_2/\text{MMT-}x\text{Ti}$  in the following. In addition,  $\text{CeO}_2$  supported on acidified MMT-H without  $\text{TiO}_2$  pillaring ( $\text{CeO}_2/\text{MMT-H}$ ),  $\text{CeO}_2$  supported on commercial  $\text{TiO}_2$  ( $\text{CeO}_2/\text{TiO}_2$ ) and traditional  $\text{V}_2\text{O}_5\text{-WO}_3/\text{TiO}_2$  catalysts, and their corresponding alkali metal-poisoned catalysts were also prepared for comparison. More details of the experimental procedures and catalysts characterization are given in the Supporting Information (SI).

**2.2.  $\text{NO}_x$  Reduction Measurements.** The catalytic activity and selectivity over the prepared catalysts were performed in a quartz fixed-bed tubular reactor (inner diameter 7 mm) with a thermocouple placed inside the catalyst bed in the temperature range of  $150\text{--}390^\circ\text{C}$ . The total gas flow rate was maintained at  $250 \text{ mL}\cdot\text{min}^{-1}$ , corresponding to the total weight hourly space velocity (WHSV) of  $50,000 \text{ mL}\cdot\text{g}^{-1}\cdot\text{h}^{-1}$ . The conversion to gas hourly space velocity (GHSV) was about  $35,000 \text{ h}^{-1}$ . The model flue gas consisted of 500 ppm of  $\text{NO}$ , 500 ppm of  $\text{NH}_3$ , 5 vol %  $\text{O}_2$ , and  $\text{N}_2$  as the balance gas. The gas concentrations of  $\text{NO}$ ,  $\text{NO}_2$ ,  $\text{NH}_3$ ,  $\text{H}_2\text{O}$ , and  $\text{N}_2\text{O}$  were simultaneously monitored by a Fourier transform infrared spectroscopy (FTIR) spectrometer (Thermo Fisher).  $\text{NO}_x$  reduction was recorded after the reaction system reached a steady state. In addition, selective catalytic reduction of  $\text{NO}_x$  over the smart catalysts in the presence of alkali (earth) metals and heavy metals was simulated by depositing alkali (earth) metal and heavy metal oxides on fresh catalysts and testing their SCR activity.

## 3. RESULTS AND DISCUSSION

**3.1.  $\text{NO}_x$  Reduction.**  $\text{NO}_x$  reduction over smart catalysts with self-created targeted antipoisoning sites was studied. First, to investigate the modification effects of Ti pillaring and  $\text{CeO}_2$  supporting on  $\text{NO}_x$  reduction and antipoisoning performance, the supporting amount of  $\text{CeO}_2$  and pillaring molar amount of  $\text{TiO}_2$  were adjusted. It was indicated that when fixing the pillaring amount of  $\text{TiO}_2$  to 6 mmol, 10 wt %  $\text{CeO}_2$  supported on MMT-6Ti showed the optimal  $\text{NO}_x$  conversion (Figure S1). Moreover, when adjusting the pillaring amount of  $\text{TiO}_2$  from 6 to 15 and 20 mmol, 10 wt %  $\text{CeO}_2$  supported on MMT-15Ti manifested higher antipoisoning ability (Figure S2). Thus, 10 wt %  $\text{CeO}_2$  supported on MMT-15Ti named 10% $\text{CeO}_2/\text{MMT-15Ti}$  was optimized to be the research target in this work, which was simplified as  $\text{CeO}_2/\text{MMT-Ti}$  hereinafter. Furthermore, it could be found that either without

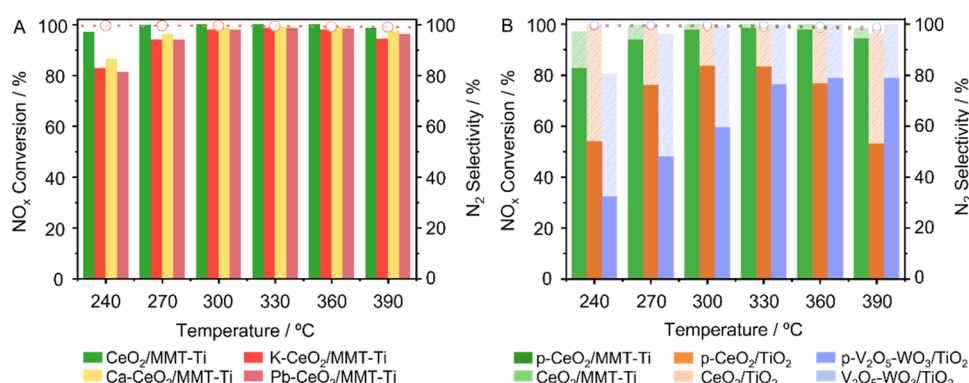


**Figure 1.** (A) Plots of NO<sub>x</sub> conversion (solid columns) and N<sub>2</sub> selectivity (dash lines) versus temperature over CeO<sub>2</sub>/MMT-Ti, K-CeO<sub>2</sub>/MMT-Ti, Ca-CeO<sub>2</sub>/MMT-Ti, and Pb-CeO<sub>2</sub>/MMT-Ti catalysts and (B) plots of NO<sub>x</sub> conversion (solid columns) and N<sub>2</sub> selectivity (dash lines) versus temperature over p-CeO<sub>2</sub>/MMT-Ti, p-CeO<sub>2</sub>/TiO<sub>2</sub>, and p-V<sub>2</sub>O<sub>5</sub>-WO<sub>3</sub>/TiO<sub>2</sub> catalysts and NO<sub>x</sub> conversion loss (dash columns) versus temperature over CeO<sub>2</sub>/MMT-Ti, CeO<sub>2</sub>/TiO<sub>2</sub>, and V<sub>2</sub>O<sub>5</sub>-WO<sub>3</sub>/TiO<sub>2</sub> catalysts after poisoning. Reaction conditions: 500 ppm of NH<sub>3</sub>, 500 ppm of NO, 5 vol % O<sub>2</sub> and balanced by N<sub>2</sub>, and WHSV of 50,000 mL·g<sup>−1</sup>·h<sup>−1</sup>.

the support of CeO<sub>2</sub> or without the pillaring of TiO<sub>2</sub>, MMT-6Ti and CeO<sub>2</sub>/MMT-H only exhibited the highest NO<sub>x</sub> conversion of 41.5 and 37.9%, respectively, which was much lower than the highest NO<sub>x</sub> conversion of CeO<sub>2</sub>/MMT-Ti, verifying the vital roles of Ti pillaring and CeO<sub>2</sub> supporting in the NO<sub>x</sub> reduction of MMT (Figure S3). Notably, the smart CeO<sub>2</sub>/MMT-Ti catalyst remained high NO<sub>x</sub> conversion after alkali metal K, alkali-earth metal Ca, and heavy metal Pb poisoning (Figure 1A), which proved its excellent antipoisoning performance. Even depositing 2 wt % K<sub>2</sub>O on the catalyst, which far exceeded the actual alkali metal content in the industrial conditions, CeO<sub>2</sub>/MMT-Ti still achieved more than 80% NO<sub>x</sub> reduction at 270–390 °C (Figure S4). Furthermore, CeO<sub>2</sub>/MMT-Ti maintained excellent NO<sub>x</sub> reduction efficiency, high N<sub>2</sub> selectivity, and a wide temperature window (300–390 °C) after K, Ca, and Pb copoisoning (Figure S5). Due to the similar poisoning mechanism and the most serious poisoning effects of alkali metal K on SCR catalysts, in the following, the alkali metal-poisoned catalyst was applied as a typical example to illustrate the antipoisoning mechanism of the smart catalyst, with the poisoned catalyst denoted p-CeO<sub>2</sub>/MMT-Ti. Figure 1B showed the NO<sub>x</sub> conversion and N<sub>2</sub> selectivity of fresh and poisoned CeO<sub>2</sub>/MMT-Ti, CeO<sub>2</sub>/TiO<sub>2</sub>, and V<sub>2</sub>O<sub>5</sub>-WO<sub>3</sub>/TiO<sub>2</sub> catalysts as a function of reaction temperature. It was clear that CeO<sub>2</sub>/MMT-Ti exhibited excellent NO<sub>x</sub> removal efficiency, with a NO<sub>x</sub> conversion of more than 80% in the temperature range of approximately 240–390 °C. After poisoning, the temperature window of p-CeO<sub>2</sub>/MMT-Ti was almost unchanged and the NO<sub>x</sub> conversion rate above 80% could be maintained at 240–390 °C. As for p-CeO<sub>2</sub>/TiO<sub>2</sub>, the highest NO<sub>x</sub> conversion decreased drastically from nearly 100% to 80% and the temperature window was also significantly narrowed to 300–330 °C. These results indicated that the TiO<sub>2</sub>-pillared MMT-supported CeO<sub>2</sub> catalyst showed comparable activity to CeO<sub>2</sub>/TiO<sub>2</sub> and the utilization of the MMT-Ti support significantly improved the poisoning resistance compared with CeO<sub>2</sub>/TiO<sub>2</sub>. Even compared with commercial V<sub>2</sub>O<sub>5</sub>-WO<sub>3</sub>/TiO<sub>2</sub> and other MMT-based catalysts,<sup>23–25</sup> CeO<sub>2</sub>/MMT-Ti still possessed greater advantages in terms of NO<sub>x</sub> reduction and antipoisoning ability. The cycling stability test was performed to check the operating stability of CeO<sub>2</sub>/MMT-Ti (Figure S6), with no significant decrease in NO<sub>x</sub> conversion observed in the three cycling stability tests even after poisoning, indicating that

CeO<sub>2</sub>/MMT-Ti was highly stable. It could be briefly concluded that the effective modification of TiO<sub>2</sub> pillaring and CeO<sub>2</sub> supporting made the CeO<sub>2</sub>/MMT-Ti catalyst possess great advantages in the application of NO<sub>x</sub> reduction with the presence of poisoning substances including alkali metals, alkali-earth metals, and heavy metals, which might be developed to be an appropriate substitute for the commercial TiO<sub>2</sub>-supported catalysts applied for NO<sub>x</sub> removal from stationary sources.

**3.2. Morphological and Structural Analyses.** To probe into the structure variation of MMT after TiO<sub>2</sub> pillaring and CeO<sub>2</sub> supporting, as well as the framework change of MMT-Ti-supported catalysts before and after poisoning, X-ray diffraction (XRD) was first used to study the crystal structure of catalysts (Figure S7). First, it could be seen that the acidified MMT exhibited a similar diffraction pattern to raw MMT, indicating that the crystal structure was not distorted by acid treatment. Besides, the small-angle XRD patterns of MMT, MMT-H, and MMT-15Ti (Figure S8) showed that raw MMT and MMT-H had a small diffraction peak at 6°, indicating the layered structure,<sup>26,27</sup> whereas the small-angle diffraction peak disappeared in the XRD pattern of MMT-15Ti, indicating that TiO<sub>2</sub> pillared into the MMT layers successfully. After further loading of CeO<sub>2</sub>, the crystal form of CeO<sub>2</sub>/MMT-Ti was almost unchanged and the peak intensity had a slight decrease when compared to that of MMT-H, indicating that the handling of loads and pillars did not break the crystal structure of MMT, while the introduction of TiO<sub>2</sub> and supporting of CeO<sub>2</sub> might lead to a slight decline of crystallinity. Beyond that, the presence of characteristic peaks of CeO<sub>2</sub> (PDF #34-0394) and TiO<sub>2</sub> (PDF #01-0562) indicated that both Ce and Ti existed in the form of oxides among CeO<sub>2</sub>/MMT-Ti. Notably, the characteristic peak position and crystallinity of the CeO<sub>2</sub>/MMT-Ti catalyst were almost unchanged after poisoning, claiming that the stable structures of Ti-pillared MMT and active CeO<sub>2</sub> compounds both had no obvious change with poison deposition. In comparison, the CeO<sub>2</sub>/TiO<sub>2</sub> catalyst owned typical diffraction of anatase TiO<sub>2</sub>, with diffraction peaks emerging at 25, 38, 48, 54, 55, and 63°. After poisoning, the crystal intensity of p-CeO<sub>2</sub>/TiO<sub>2</sub> suffered an obvious decrease, which might result from the poison deposition on the catalyst surface. However, the negligible change of crystal phase and intensity of CeO<sub>2</sub>/MMT-Ti after poisoning likely



declared that poisoning cations could be well stored in the framework of MMT-Ti.

In addition, scanning electron microscopy (SEM) images (Figure S9) illustrated that CeO<sub>2</sub>/MMT-Ti had a peeling layered structure, which was derived from the natural MMT carrier, but CeO<sub>2</sub>/TiO<sub>2</sub> presented a large block structure, which was likely detrimental to the poisoning substances storage and resistance promotion. Simultaneously, it could be seen that there was no distinct change in SEM images of CeO<sub>2</sub>/MMT-Ti and CeO<sub>2</sub>/TiO<sub>2</sub> after poisoning. The scanning electron microscope equipped with energy dispersive spectroscopy (SEM-EDS) mapping results of CeO<sub>2</sub>/MMT-Ti, p-CeO<sub>2</sub>/MMT-Ti, CeO<sub>2</sub>/TiO<sub>2</sub>, and p-CeO<sub>2</sub>/TiO<sub>2</sub> (Figures S10–S13) exhibited that all catalysts had a uniform distribution of the active component Ce. In addition, the pillared Ti also dispersed well in the framework of MMT among CeO<sub>2</sub>/MMT-Ti and p-CeO<sub>2</sub>/MMT-Ti catalysts, indicating the effective pillaring of Ti into the interlayers. Furthermore, it could be seen from the element ratio summary of each catalyst (Table S1) that the ratio of K on p-CeO<sub>2</sub>/MMT-Ti (0.64) was lower than that on p-CeO<sub>2</sub>/TiO<sub>2</sub> (0.70), indicating that part of poisoning cations on p-CeO<sub>2</sub>/MMT-Ti might be effectively anchored between the catalyst layers, which would show fewer poisoning effects on active CeO<sub>2</sub> and be conducive to the excellent poisoning resistance. As shown in the transmission electron microscopy (TEM) and high-resolution TEM (HRTEM) images, the MMT still maintained the layer structure after TiO<sub>2</sub> pillaring and CeO<sub>2</sub> supporting and the CeO<sub>2</sub> [111] crystal plane was clearly seen, indicating that the Ce element existed on the catalyst in the form of oxides (Figure S14A,B). In addition, it could be seen from the EDS line scan results that TiO<sub>2</sub> was successfully pillared into the MMT interlayer (Figure S14C,D).

In terms of porous structure analysis, it could be found that after acid treatment, the specific surface area of MMT-H increased sharply (Table S2), which was probably due to the expansion of the interlayer spacing caused by the insertion of H<sub>2</sub>O molecules into MMT. After the successive treatments of TiO<sub>2</sub> pillaring and CeO<sub>2</sub> supporting, the surface area had a slight decrease, which was likely attributable to the deposition of TiO<sub>2</sub> and CeO<sub>2</sub>. With the introduction of poisoning substances, the specific surface area and pore volume of p-CeO<sub>2</sub>/MMT-Ti slightly decreased from 211.6 to 183.1 m<sup>2</sup>·g<sup>−1</sup> and from 0.19 to 0.17 cm<sup>3</sup>·g<sup>−1</sup>, respectively, while the pore size slightly increased from 4.5 to 4.6 nm. As for CeO<sub>2</sub>/TiO<sub>2</sub>, the specific surface area and pore volume reduced more severely from 121.1 to 87.4 m<sup>2</sup>·g<sup>−1</sup> and from 0.37 to 0.27 cm<sup>3</sup>·g<sup>−1</sup>, respectively, and the pore size increased more obviously from 11.4 to 11.6 nm after poisoning. This phenomenon was likely due to the alkali metal oxides covering the CeO<sub>2</sub>/TiO<sub>2</sub> catalyst surface, but most of the poisoning cations would be effectively anchored into the interlayers of CeO<sub>2</sub>/MMT-Ti to avoid the poisoning of active CeO<sub>2</sub>. Above all, it could be learned that the acid treatment and Ti pillaring could well maintain the special layered structure of MMT, which provided abundant fixing sites for poisoning substances after supporting active CeO<sub>2</sub>, while the CeO<sub>2</sub> exposed on the surface of TiO<sub>2</sub> would be severely attacked by poisoning cations, which revealed the significant role of the modified MMT-Ti support in the improvement of antipoisoning performance.

**3.3. Surface Acidity and Redox Capacity.** NH<sub>3</sub> temperature-programmed desorption mass spectra (NH<sub>3</sub>-TPD-MS) were used to study the surface acidity and quantify

the acid amount of as-prepared catalysts, with the results demonstrated in Figure 2A. The MS signals for each catalyst

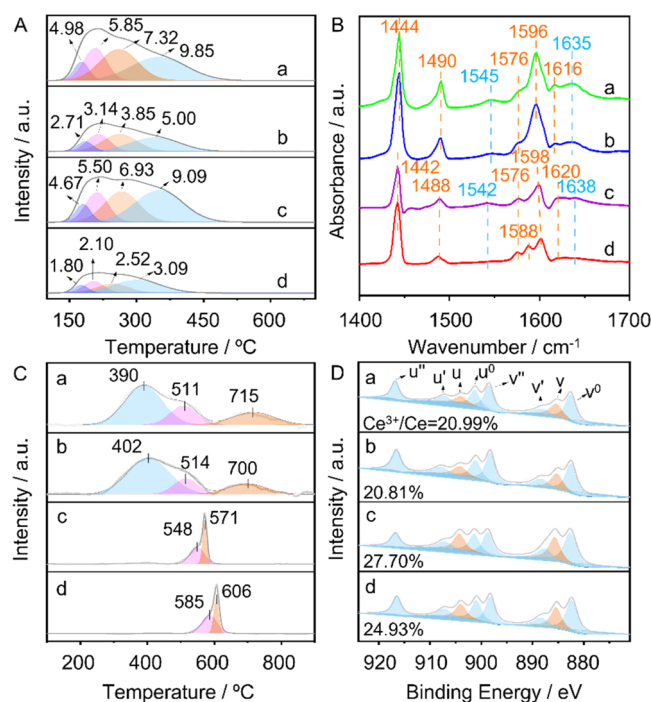


**Figure 2.** (A) NH<sub>3</sub>-TPD-MS profiles, (B) Py-FTIR spectra, (C) hydrogen temperature-programmed reduction (H<sub>2</sub>-TPR) profiles, and (D) X-ray photoelectron spectrometry (XPS) spectra of Ce 3d for (a) CeO<sub>2</sub>/MMT-Ti, (b) p-CeO<sub>2</sub>/MMT-Ti, (c) CeO<sub>2</sub>/TiO<sub>2</sub>, and (d) p-CeO<sub>2</sub>/TiO<sub>2</sub> catalysts.

were divided into four peaks, among which the desorption peaks below 200 °C represented weak acid sites, those at 200–400 °C represented medium-strong acid sites, and those above 400 °C represented strong acid sites.<sup>14,28</sup> It was observed that four NH<sub>3</sub> desorption peaks located at 177, 208, 260, and 350 °C emerged in the profile of CeO<sub>2</sub>/MMT-Ti. As for CeO<sub>2</sub>/TiO<sub>2</sub>, similar desorption peaks were also apparent at 180, 212, 267, and 350 °C. By integrating desorption peak areas, the calculated acid quantity of CeO<sub>2</sub>/MMT-Ti (28.0 μmol·g<sup>−1</sup>) was almost the same as that of CeO<sub>2</sub>/TiO<sub>2</sub> (26.2 μmol·g<sup>−1</sup>) (Table S3), indicating the similar NH<sub>3</sub> adsorption behavior and amount over these two fresh catalysts. After poisoning, desorption peak positions had a negligible change over p-CeO<sub>2</sub>/MMT-Ti and p-CeO<sub>2</sub>/TiO<sub>2</sub> when compared to fresh ones, respectively, while the calculated acid loss was different. It was found that the loss ratio of p-CeO<sub>2</sub>/MMT-Ti (47.41%) was significantly less than that of p-CeO<sub>2</sub>/TiO<sub>2</sub> (63.94%) (Table S3), indicating that the poisoning effect on the acid amount of CeO<sub>2</sub>/MMT-Ti was smaller. Furthermore, it could be deduced that the less acid loss might be due to the effective anchoring of poisoning cations into the interlayers of MMT-Ti, which accounted for the more excellent poisoning resistance of CeO<sub>2</sub>/MMT-Ti.<sup>29</sup> As compared with the NH<sub>3</sub>-TPD-MS profile of CeO<sub>2</sub>/MMT-H (Figure S15), the strong acid peak at 456 °C disappeared after TiO<sub>2</sub> pillaring into the layers of the MMT support, indicating that TiO<sub>2</sub> might combine with Si or Al hydroxyl sites of MMT-H that provided strong acid sites within the high-temperature range. Simultaneously, the desorption peak at a higher temperature of 350 °C appeared among CeO<sub>2</sub>/MMT-Ti also encountered an obvious decline

after poisoning, reflecting that this part of medium-strong acid sites mainly derived from pillared  $\text{TiO}_2$  would express a certain combining effect with poisoning substances, thus protecting the active  $\text{CeO}_2$  from poisoning together with the intrinsic trapping sites of MMT. Meanwhile, the desorption peak area of  $\text{CeO}_2$ /MMT-H was significantly larger than that of  $\text{CeO}_2$ /MMT, indicating that acid treatment could indeed increase the total acid amount of the catalyst (Figure S15 and Table S3). The loss of acid amount on the surface of  $\text{CeO}_2$ /MMT-Ti after poisoning was significantly smaller than that of  $\text{CeO}_2$ /TiO<sub>2</sub>, indicating that there were relevant sites on the MMT support that were preferentially bound to the poisoning metal cations, thus protecting the  $\text{NH}_3$  adsorption sites on the catalyst.

FTIR spectra of pyridine desorption (Py-FTIR) shown in Figure 2B were recorded to accurately characterize the acid types of catalysts. For  $\text{CeO}_2$ /MMT-Ti, bands at 1444, 1490, 1576, 1596, and 1616  $\text{cm}^{-1}$  corresponded to the adsorption of pyridine on Lewis acid sites and those at 1545 and 1635  $\text{cm}^{-1}$  were assigned to the adsorption of pyridine on Brønsted acid sites, which was consistent with the phenomenon observed for  $\text{CeO}_2$ /MMT-H (Figure S16B).<sup>14,30,31</sup> This indicated that  $\text{CeO}_2$ /MMT-Ti and  $\text{CeO}_2$ /MMT-H had the same acid types. As for  $\text{CeO}_2$ /TiO<sub>2</sub>, peaks at 1442, 1488, 1576, 1598, and 1620  $\text{cm}^{-1}$  resulted from the adsorption of pyridine on Lewis acid sites, and those at 1542 and 1638  $\text{cm}^{-1}$  originated from the adsorption of pyridine on Brønsted acid sites.<sup>22,31,32</sup> The peak positions observed for  $\text{CeO}_2$ /MMT-Ti and  $\text{CeO}_2$ /TiO<sub>2</sub> were basically the same, but  $\text{CeO}_2$ /MMT-Ti had an obviously higher intensity compared with the latter. It indicated that Ti pillaring into MMT had little impact on the acid types, while it greatly improved the total amount of acid sites on  $\text{CeO}_2$ /MMT-Ti, which was consistent with  $\text{NH}_3$ -TPD-MS results. The increased Brønsted acid sites were mainly obtained by the acidification of MMT and part of the Brønsted acid could be converted into Lewis acid under calcining conditions, which eventually increased the Lewis acid on MMT-Ti. As for poisoned catalysts, the surface acid species of these two catalysts did not change, but the Brønsted acid peak intensity of p- $\text{CeO}_2$ /TiO<sub>2</sub> decreased more drastically. In contrast, the influence of alkali metals on the acid quantity and intensity of the  $\text{CeO}_2$ /MMT-Ti catalyst was limited, so more acid centers, especially Brønsted acid centers, could effectively act as the trapping sites to anchor poisoning cations, which protected the active  $\text{CeO}_2$  centers and improved the poisoning resistance of catalysts.

Hydrogen temperature-programmed reduction ( $\text{H}_2$ -TPR) was carried out to study the redox properties of catalysts, with the results shown in Figure 2C. For  $\text{CeO}_2$ /MMT-Ti, peaks at 390 and 511 °C represented the reduction of  $\text{Ce}^{4+}$  and  $\text{Ce}^{4+}\text{-O-Ce}^{3+}$  species on the surface, while that at 715 °C belonged to the reduction of  $\text{Ce}^{4+}$  species in the bulk phase.<sup>33–35</sup> Compared with  $\text{CeO}_2$ /MMT-H (Figure S17B), reduction peaks of surface Ce species on  $\text{CeO}_2$ /MMT-Ti split into two peaks and the ratio of surface to bulk reduction increased, indicating that  $\text{Ce}^{4+}$  was more easily reduced with the pillaring of TiO<sub>2</sub> and thus improved the  $\text{NO}_x$  reduction activity. As for  $\text{CeO}_2$ /TiO<sub>2</sub>, only two reduction peaks appeared at 548 and 571 °C, representing the reduction of  $\text{Ce}^{4+}\text{-O-Ce}^{3+}$  species on the surface and  $\text{Ce}^{4+}$  species in the bulk phase. For the fresh  $\text{CeO}_2$ /MMT-Ti catalyst, the reduction temperature of all surface Ce species was lower than that of the  $\text{CeO}_2$ /TiO<sub>2</sub> catalyst, indicating that superficial Ce species on  $\text{CeO}_2$ /MMT-Ti was easier to be reduced and the redox performance of

$\text{CeO}_2$ /MMT-Ti had been improved compared with that of  $\text{CeO}_2$ /TiO<sub>2</sub>. After poisoning, the reduction peak of  $\text{CeO}_2$ /MMT-Ti only slightly shifted toward high temperature, manifesting that the introduction of poisoning cations had little effect on the redox property. As for p- $\text{CeO}_2$ /TiO<sub>2</sub>, the  $\text{H}_2$  reduction peak of surface  $\text{Ce}^{4+}\text{-O-Ce}^{3+}$  species shifted about 40 °C to a higher temperature, indicating the severe damage of poisoning to the redox ability of  $\text{CeO}_2$ /TiO<sub>2</sub>. This also explained why  $\text{CeO}_2$ /TiO<sub>2</sub> became less active after poisoning. The use of MMT support reduced the effect of poisoning metal cations on the active Ce species of  $\text{CeO}_2$ /MMT-Ti, indicating that the presence of relevant antipoisoning sites on the MMT support protected the active species on the catalyst. This result was also consistent with the results of  $\text{NH}_3$ -TPD-MS.

The surface element composition and valence changes before and after poisoning were further detected by X-ray photoelectron spectrometry (XPS). The peaks of Ce 3d spectra marked as  $v$  and  $u$  were on behalf of the  $\text{Ce}^{3+}$  species, while other peaks tagged as  $v^0$ ,  $v'$ ,  $v''$ ,  $u^0$ ,  $u'$ , and  $u''$  represented the  $\text{Ce}^{4+}$  species, as shown in Figure 2D.<sup>7,10</sup> For  $\text{CeO}_2$ /MMT-Ti, the pillaring of TiO<sub>2</sub> significantly increased the proportion of  $\text{Ce}^{3+}$  compared with that for  $\text{CeO}_2$ /MMT-H (Figure S18), which also highly accounted for the enhanced  $\text{NO}_x$  conversion of  $\text{CeO}_2$ /MMT-Ti than  $\text{CeO}_2$ /MMT-H that was caused by the effective TiO<sub>2</sub> pillaring. After poisoning, the proportion of  $\text{Ce}^{3+}$  on  $\text{CeO}_2$ /MMT-Ti remained almost unchanged, whereas that of p- $\text{CeO}_2$ /TiO<sub>2</sub> decreased significantly. This reflected that the poisoning cations scarcely influenced the redox capability and valence distribution of  $\text{Ce}^{3+}$  on p- $\text{CeO}_2$ /MMT-Ti, which was due to the fact that the abundant ion-exchange sites and pillared Ti species between the layers of the MMT-Ti support preferentially bound to poisoning cations compared to the bulk TiO<sub>2</sub> support so that the active components were protected. In addition, the elemental content data from XPS and SEM-EDS were used to analyze the proportion of K element on the catalyst surface and in the near-bulk phase to infer whether K poisoned the active component  $\text{CeO}_2$  on the surface or bound to the interlayer antipoisoning sites. It was found the K element content on the surface of p- $\text{CeO}_2$ /MMT-Ti was lower than that of p- $\text{CeO}_2$ /TiO<sub>2</sub> corresponding to the results of XPS and SEM-EDS mapping (Figure S19), indicating that poisoning cations might be captured by the Brønsted acid sites and pillared Ti species between the MMT-Ti layers in  $\text{CeO}_2$ /MMT-Ti, whereas the poisons mainly deposited on the surface of  $\text{CeO}_2$ /TiO<sub>2</sub>, which affected the valence state of Ce and eventually reduced the catalytic activity of the catalyst.

As for the O 1s XPS spectra of  $\text{CeO}_2$ /MMT-Ti (Figure S20), the peak at 532.37 eV represented the surface adsorbed oxygen ( $\text{O}_a$ ) and the other one at 529.97 eV was assigned to the lattice oxygen ( $\text{O}_\beta$ ).<sup>36</sup> Noticeably, the calculated  $\text{O}_a/(\text{O}_a + \text{O}_\beta)$  ratio of  $\text{CeO}_2$ /MMT-Ti (67.8%) was significantly higher than that of  $\text{CeO}_2$ /TiO<sub>2</sub> (18.5%), evidencing the existence of more oxygen vacancies on the  $\text{CeO}_2$ /MMT-Ti catalyst. Combined with the O 1s spectra of  $\text{CeO}_2$ /MMT-H (Figure S21), the  $\text{O}_a$  on  $\text{CeO}_2$ /MMT-Ti was mainly derived from the MMT support, rather than the pillared TiO<sub>2</sub>. After poisoning, the active  $\text{O}_a$  content of p- $\text{CeO}_2$ /MMT-Ti was barely changed compared with that of the fresh one, indicating that the introduction of poisoning substances hardly attacked the surface-active species but was effectively anchored by the intrinsic  $-\text{OH}$  sites and pillared Ti species of MMT-Ti. In

comparison, the surface  $O_{\alpha}$  content of  $CeO_2/TiO_2$  was much lower than that of  $CeO_2/MMT-Ti$  and it decreased distinctly after poisoning compared with  $CeO_2/MMT-Ti$ , indicating that poisoning substances had a greater influence on  $O_{\alpha}$  of  $CeO_2/TiO_2$ , which was also one of the reasons for its  $NO_x$  conversion degradation after poisoning. To sum up, the XPS spectra of Ce 3d and O 1s also yielded similar results to the  $H_2$ -TPR profiles, indicating that the use of MMT support protected the active  $Ce^{3+}$  species and the chemisorbed oxygen species  $O_{\alpha}$  on the catalyst surface.

As for the XPS spectra of Ti 2p (Figure S22),<sup>37,38</sup> it could be seen that peaks of  $CeO_2/MMT-Ti$  were shifted to low binding energy after poisoning, further showing that Ti indeed possessed a certain protective effect on the active components from poisoning substance attacking. In terms of the XPS Si 2p and Al 2p spectra of  $CeO_2/MMT-Ti$  (Figures S23 and S24), no obvious change was found before and after poisoning, which could not reveal whether poison interacted with Si or Al of the MMT-Ti carrier, and further proof was needed.

### 3.4. Antipoisoning Process and Reactant Adsorption.

The chemical environments of Si and Al in fresh and poisoned  $CeO_2/MMT-Ti$  catalysts were studied by solid-state NMR spectra. Figure 3A,B depicted the  $^{29}Si$  and  $^{27}Al$  NMR spectra of

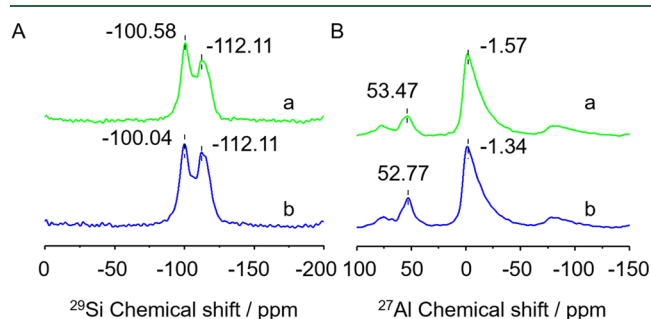


**Figure 3.** Solid-state (A)  $^{29}Si$  and (B)  $^{27}Al$  MAS NMR of (a)  $CeO_2/MMT-Ti$  and (b)  $p-CeO_2/MMT-Ti$  catalysts.

$CeO_2/MMT-Ti$  and  $p-CeO_2/MMT-Ti$ . The  $^{29}Si$  NMR spectra exhibited different frame Si  $Q^4$  environments of  $CeO_2/MMT-Ti$ , namely, Si (4Si, 0Al) [ $-112.11$  ppm] and Si (3Si, 1Al) [ $-100.58$  ppm].<sup>39,40</sup> As for the  $^{27}Al$  NMR spectra shown in Figure 3B, the main peak near  $-1.57$  ppm was distributed to octahedrally coordinated Al, and the small peak at  $53.47$  ppm was attributed to tetrahedrally coordinated Al.<sup>40,41</sup> The small peak might originate from the acid treatment and calcination of the MMT support, which was relatively active in the  $NO_x$  reduction and poisoning resistance. When compared with the  $^{29}Si$  and  $^{27}Al$  NMR spectra of  $CeO_2/MMT-H$  (Figure S25), it was observed that Ti pillaring made the chemical shift of Si and Al both move toward the lower side, indicating that the strong interaction between Ce and Ti after the introduction of Ti shifted the peaks of Si and Al and improved the  $NO_x$  reduction activity of  $CeO_2/MMT-Ti$ . After poisoning, the small peak at  $53.47$  ppm among  $^{27}Al$  NMR spectra shifted toward the low chemical shift, which was due to the increase of electron cloud density around the tetrahedral Al core, indicating that poisoning substances would bond to the four-coordinated Al sites. By contrast, the peak at  $-1.57$  ppm remained almost unchanged, indicating that the chemical environment of the eight-coordinated Al did not change. As for the  $^{29}Si$  NMR spectra after poisoning, the peak at  $-112.11$  ppm for  $CeO_2/MMT-Ti$  did not change, while the peak at  $-100.58$  ppm

shifted to  $-100.04$  ppm, demonstrating that poisoning substances indirectly affected Si around Al by combining with the adjacent Al sites. These findings further revealed that poisoning cations were mainly bound to the inherently active tetrahedral coordination Al sites between the MMT layers, rather than the eight-coordinated Al and framed Si sites. As a result, MMT released the combination of poisoning substances with the active Ce sites and significantly improved the poisoning resistance of the  $CeO_2/MMT-Ti$  catalyst. The solid-state NMR spectra further verified the inference of  $NH_3$ -TPD and  $H_2$ -TPR that the self-created targeted antipoisoning sites on the MMT support were the tetrahedral coordination Al sites.

Under the special protective effects of framed tetrahedral coordination Al sites and pillared Ti species, the adsorption and activation behaviors of  $NH_3$  and  $NO_x$  reactants would be differential over MMT-H- and  $TiO_2$ -supported catalysts. Thus, *in situ* diffuse reflectance infrared Fourier transform spectroscopy (DRIFTS) of  $NH_3$  desorption (Figures S26–S28) was first carried out to characterize the behaviors of adsorbed  $NH_3$  species. For  $CeO_2/MMT-Ti$  (Figure S26A), adsorption peaks of  $NH_4^+$  and  $NH_3$  species were observed clearly, while an additional peak at  $1284$   $cm^{-1}$  was attributed to  $NH_3$  coordinated to Lewis acid sites for  $CeO_2/MMT-H$  (Figure S27).<sup>42</sup> However, this peak disappeared after  $TiO_2$  pillaring, indicating that  $TiO_2$  occupied the Lewis acid sites of MMT, which corresponded to the result of  $NH_3$ -TPD-MS. As for  $p-CeO_2/MMT-Ti$  (Figure S26B), the peak at  $1592$   $cm^{-1}$  disappeared and a new peak appeared at  $1601$   $cm^{-1}$  corresponding to the adsorption of  $NH_3$  on the Lewis acid sites.<sup>43</sup> Meanwhile, acid type and acid intensity of  $p-CeO_2/MMT-Ti$  did not change significantly, which was consistent with the fact that the activity of  $CeO_2/MMT-Ti$  did not obviously decrease after poisoning. In comparison, the  $NH_3$  adsorption peak of  $CeO_2/TiO_2$  was still obvious in the temperature range of  $250$ – $300$   $^{\circ}C$ , indicating that the  $NH_3$  adsorbed on  $CeO_2/TiO_2$  could be maintained at a higher temperature. Therefore, it could be inferred that  $NH_3$  adsorbed on medium-strong Lewis acid sites played an important role in the  $CeO_2/TiO_2$  catalyst. However,  $NH_3$  adsorption peaks of  $CeO_2/TiO_2$  above  $200$   $^{\circ}C$  almost disappeared after poisoning (Figure S28B), indicating that poisoning substances had a great influence on the acid sites, especially Lewis acid sites. In addition, it was noticed that the peak at  $1300$   $cm^{-1}$  disappeared after poisoning and a new peak at  $1181$   $cm^{-1}$  belonging to  $NH_3$  adsorbed on Lewis acid sites appeared simultaneously. This indicated that the active centers of  $CeO_2/TiO_2$  were affected by poisoning cations, which declined the  $NO_x$  conversion of  $CeO_2/TiO_2$  severely. These results strongly suggested that  $CeO_2/MMT-Ti$  possessed stronger acidity and was not affected by poisoning substances simply, which mainly resulted from the protective effects of tetrahedral coordination Al sites and pillared Ti species, thus ensuring the promoted poisoning resistance.

*In situ* DRIFTS of  $NO + O_2$  desorption (Figures S29–S31) was used to investigate the  $NO_x$  species adsorbed on catalysts. There were more  $NO_x$  species on  $CeO_2/MMT-Ti$  (Figure S29A) compared with those on  $CeO_2/MMT-H$  (Figure S30), indicating that  $TiO_2$  pillaring enhanced  $NO_x$  adsorption. After poisoning, a quite weak band at  $1397$   $cm^{-1}$  assigned to less active trans- $(NO)_2$  appeared for  $p-CeO_2/MMT-Ti$  (Figure S29B),<sup>22</sup> which would express little influence of poisons on  $p-CeO_2/MMT-Ti$ . Meanwhile, it could be seen that the



adsorption peak of bidentate nitrate species on  $\text{CeO}_2/\text{MMT-Ti}$  declined and tended to disappear with the temperature increasing, while the adsorption capacity of active monodentate nitrate species increased over  $\text{p-CeO}_2/\text{MMT-Ti}$ , indicating that the bidentate nitrate was converted into monodentate nitrate that was easier to desorb and activate. As for  $\text{CeO}_2/\text{TiO}_2$  and  $\text{p-CeO}_2/\text{TiO}_2$  (Figure S31), it could be found that the peak intensity of adsorbed  $\text{NO}_x$  species increased significantly after poisoning, which might be caused by the deposition of poisoning metal oxides, but these adsorbed  $\text{NO}_x$  species were very stable and not easy to be activated. Simultaneously, the desorption temperature of  $\text{NO}_x$  species increased, which further proved that the adsorbed nitrate species after poisoning was more stable and difficult to participate in the reaction. Further, the peak of active bridge nitrate at  $1606\text{ cm}^{-1}$  was still obvious when the temperature increased to  $300\text{ }^\circ\text{C}$  over  $\text{p-CeO}_2/\text{TiO}_2$ , confirming the more thermal stable property that was adverse to the successive reaction. In addition, peaks representing linear nitrate ( $1441\text{ cm}^{-1}$ ) and bridge nitrate ( $1253\text{--}1248\text{ cm}^{-1}$ ) disappeared and were replaced by a peak of trans- $(\text{NO})_2$  species ( $1397\text{ cm}^{-1}$ ), which was more stable and not toilless to desorb,<sup>22</sup> whereas the peak of stable bidentate nitrate species remained steady. From these results, it could be seen that good maintenance of active nitrate species and less accumulation of inactive nitrate species on  $\text{CeO}_2/\text{MMT-Ti}$  after poisoning would guarantee the successive reaction and thus promoted the poisoning resistance. It is noted that the targeted tetrahedral coordination Al sites of  $\text{CeO}_2/\text{MMT-Ti}$  anchored the poisoning metal cations, thus maintaining the normal adsorption and activation of  $\text{NH}_3$  and  $\text{NO}_x$  on the catalyst surface. These results were also consistent with the efficient maintenance of catalyst acidity and redox properties shown by  $\text{NH}_3$ -TPD profiles,  $\text{H}_2$ -TPR profiles, and XPS spectra.

**3.5. Reaction Mechanism Study.** To explore the reaction pathways and mechanisms, transient *in situ* DRIFTS experiments were carried out, as shown in Figure 4. After 1 h with

$\text{NH}_3$  pretreatment at  $240\text{ }^\circ\text{C}$ , peaks appearing at  $1675$  and  $1434\text{ cm}^{-1}$  were attributed to  $\text{NH}_4^+$  coordinated with Brønsted acid sites<sup>44,45</sup> and that at  $1578\text{ cm}^{-1}$  was assigned to  $\text{NH}_3$  coordinated with Lewis acid sites<sup>46</sup> for  $\text{CeO}_2/\text{MMT-Ti}$  (Figure 4A). Comparatively, similar  $\text{NH}_3$  species adsorption peaks appeared on  $\text{CeO}_2/\text{MMT-Ti}$  and  $\text{CeO}_2/\text{TiO}_2$  (Figure S32A). Furthermore, with the introduction of  $\text{NO}$  and  $\text{O}_2$ , two bands generated gradually at  $1535$  and  $1367\text{ cm}^{-1}$ , representing monodentate nitrate<sup>47</sup> and nitrate species intermediate<sup>48</sup> for  $\text{CeO}_2/\text{MMT-Ti}$ , respectively, and two peaks appeared at  $1605$  and  $1514\text{ cm}^{-1}$  on behalf of bridge nitrate<sup>49</sup> and monodentate nitrate for  $\text{CeO}_2/\text{TiO}_2$ , respectively.<sup>50</sup> It could be found that the  $\text{NH}_3$  adsorption peak of  $\text{CeO}_2/\text{MMT-Ti}$  disappeared more slowly than  $\text{CeO}_2/\text{TiO}_2$ , manifesting that  $\text{CeO}_2/\text{MMT-Ti}$  adsorbed more  $\text{NH}_3$  species with more acid sites, as  $\text{NH}_3$ -TPD-MS results revealed. As for  $\text{p-CeO}_2/\text{MMT-Ti}$  (Figure 4B), similar  $\text{NH}_3$  adsorption peaks at  $1675$  and  $1447\text{ cm}^{-1}$  attributed to  $\text{NH}_4^+$  coordinated with Brønsted acid sites and  $1596\text{ cm}^{-1}$  assigned to  $\text{NH}_3$  bound to Lewis acid sites emerged. With the introduction of  $\text{NO}$  and  $\text{O}_2$ , adsorbed ammonia species disappeared quickly and were replaced by nitrate peaks, including the clear bridge nitrate peak at  $1605\text{ cm}^{-1}$ , bidentate nitrate peak at  $1575\text{ cm}^{-1}$ , and monodentate nitrate peak at  $1528\text{ cm}^{-1}$ , which was easy to be activated and participated in the  $\text{NH}_3$ -SCR reaction. However, for  $\text{p-CeO}_2/\text{TiO}_2$  (Figure S32B), the  $\text{NH}_3$  adsorption amount was obviously decreased. What is more, the  $\text{NH}_3$  consumption rate was significantly slower than that of the fresh sample for  $\text{p-CeO}_2/\text{TiO}_2$ , which was not conducive to the SCR reaction. Meanwhile, with the introduction of  $\text{NO} + \text{O}_2$ , the peak intensity of bridge nitrate on  $\text{p-CeO}_2/\text{TiO}_2$  was visibly weaker than those on  $\text{p-CeO}_2/\text{MMT-Ti}$ , while bidentate nitrate and inert  $\text{N}_2\text{O}_2^{2-}$  species formed and accumulated within 30 min, which would gradually hinder the following surface reaction.

After  $\text{NO} + \text{O}_2$  pretreatment for 1 h at  $240\text{ }^\circ\text{C}$ , both  $\text{CeO}_2/\text{MMT-Ti}$  (Figure 4C) and  $\text{CeO}_2/\text{TiO}_2$  (Figure S33A) showed adsorption peaks of  $\text{NO}_x$ . In more detail, the peaks at  $1605$ ,  $1535$ , and  $1360\text{ cm}^{-1}$  were attributed to bridge nitrate, monodentate nitrate, and bidentate nitrate for  $\text{CeO}_2/\text{MMT-Ti}$ .<sup>41,47,49</sup> After the introduction of  $\text{NH}_3$ , adsorption peaks were basically consistent with those observed in the *in situ* DRIFTS data of  $\text{NH}_3$  preadsorption for  $\text{CeO}_2/\text{MMT-Ti}$  and  $\text{CeO}_2/\text{TiO}_2$ , except for that at  $1471\text{ cm}^{-1}$  attributed to  $\text{NH}_4^+$  coordinated with Brønsted acid sites. However, nitrate species of  $\text{CeO}_2/\text{MMT-Ti}$  reacted more quickly with  $\text{NH}_3$  and the successive adsorption of  $\text{NH}_3$  was also stronger. After poisoning, although  $\text{p-CeO}_2/\text{MMT-Ti}$  lacked a peak of  $\text{NH}_4^+$  adsorbing on the Brønsted acid sites ( $1434\text{ cm}^{-1}$ ), the strength of peaks at  $1675$  and  $1578\text{ cm}^{-1}$  representing  $\text{NH}_4^+$  bound to Brønsted acid sites and  $\text{NH}_3$  coordinated to Lewis acid sites was enhanced (Figure 4D). In addition, the consumption of nitrate species on  $\text{p-CeO}_2/\text{MMT-Ti}$  at  $1665$ ,  $1560$ ,  $1380$ , and  $1369\text{ cm}^{-1}$  assigned to bridge nitrate, bidentate nitrate, bidentate nitrate, and  $\text{N}_2\text{O}_2^{2-}$  species was significantly faster than that on  $\text{p-CeO}_2/\text{TiO}_2$ , indicating that  $\text{NO}_x$  species adsorbed on  $\text{p-CeO}_2/\text{MMT-Ti}$  were more active and easily participated in the  $\text{NH}_3$ -SCR reaction. On the contrary, the amount of adsorbed nitrate species on  $\text{p-CeO}_2/\text{TiO}_2$  greatly increased compared with that on the fresh sample, but most of them were inactive and could not be effectively consumed by  $\text{NH}_3$  so that there were still obvious adsorption peaks after  $\text{NH}_3$  was injected for 30 min (Figure S33B). This was due to the fact that the inert nitrate species adsorbed by

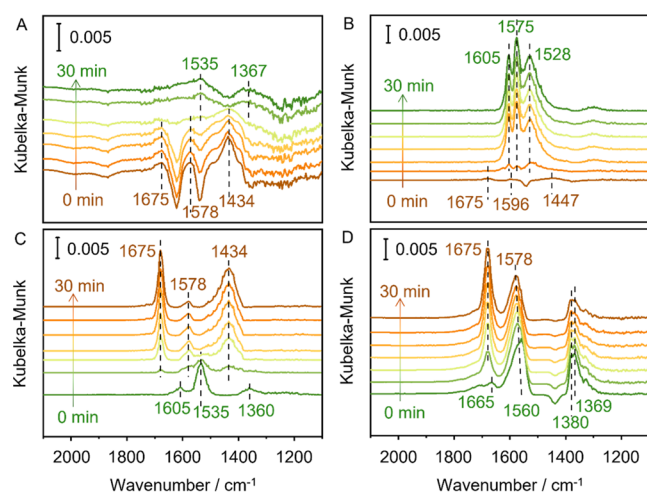


**Figure 4.** *In situ* DRIFTS of the transient reaction upon passing  $\text{NO} + \text{O}_2$  over (A)  $\text{CeO}_2/\text{MMT-Ti}$  and (B)  $\text{p-CeO}_2/\text{MMT-Ti}$  catalysts with  $\text{NH}_3$  preadsorbed at  $240\text{ }^\circ\text{C}$  as a function of time. *In situ* DRIFTS of the transient reaction upon passing  $\text{NH}_3$  over (C)  $\text{CeO}_2/\text{MMT-Ti}$  and (D)  $\text{p-CeO}_2/\text{MMT-Ti}$  catalysts with  $\text{NO} + \text{O}_2$  preadsorbed at  $240\text{ }^\circ\text{C}$  as a function of time. Reaction conditions:  $1000\text{ ppm}$  of  $\text{NO}$  and  $1000\text{ ppm}$  of  $\text{NO} + 5\text{ vol } \%$   $\text{O}_2$  with  $\text{N}_2$  as the balance gas.

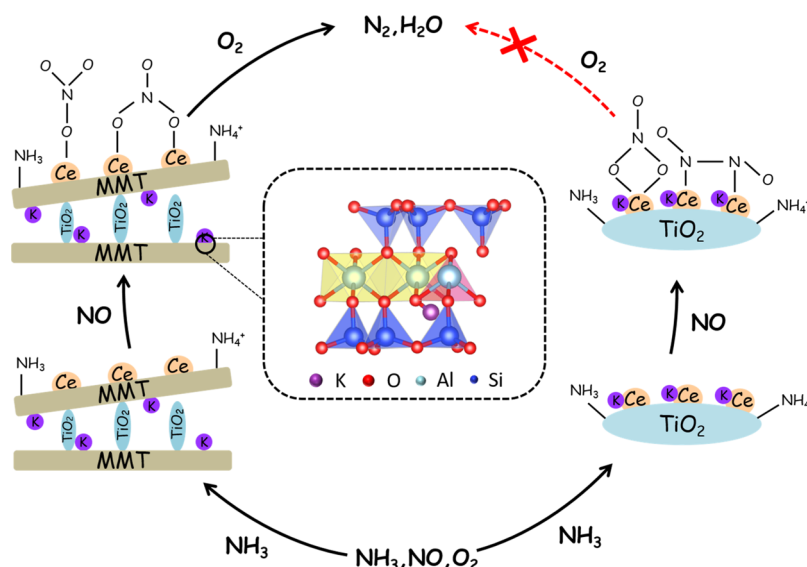


**Figure 5.** Schematic illustration of poisoning and antipoisoning mechanisms over p-CeO<sub>2</sub>/MMT-Ti and p-CeO<sub>2</sub>/TiO<sub>2</sub> catalysts for NO<sub>x</sub> reduction.

alkali metal oxides on the surface of p-CeO<sub>2</sub>/TiO<sub>2</sub> almost did not participate in the reaction. Simultaneously, the adsorption of NH<sub>3</sub> on p-CeO<sub>2</sub>/TiO<sub>2</sub> was greatly weakened and the peak at 1471 cm<sup>-1</sup> (NH<sub>3</sub> adsorbing on the Brønsted acid sites)<sup>S1</sup> was lost, which proved that poisoning substances had a serious effect on the acidity of CeO<sub>2</sub>/TiO<sub>2</sub>. Based on the above results, for CeO<sub>2</sub>/MMT-Ti and CeO<sub>2</sub>/TiO<sub>2</sub>, whether fresh or poisoned, the adsorbed NH<sub>3</sub> and NO<sub>x</sub> could be consumed after the introduction of another reactant and the adsorption of the other reactant could be clearly observed at the same time, showing a typical Langmuir-Hinshelwood mechanism. The difference emerged after poisoning, which was because the reaction path over the p-CeO<sub>2</sub>/TiO<sub>2</sub> surface was hindered and the consumption of NO<sub>x</sub> species became quite slow, while the reaction still smoothly occurred over p-CeO<sub>2</sub>/MMT-Ti via the rapid interaction of adsorbed NH<sub>3</sub> and NO<sub>x</sub> species without the influence of poisons.

In summary, NO<sub>x</sub> reduction over smart catalysts with self-created targeted antipoisoning sites has been originally demonstrated. Combining a series of characterizations, more acid sites, higher active oxygen species, and better redox ability were proved to be highly conducive to the superior NO<sub>x</sub> removal efficiency. Probing the antipoisoning mechanism of the smart catalyst, it was found the intrinsic trapping sites of MMT together with pillared TiO<sub>2</sub> expressed a specific combining effect on poisoning substances to prevent the active species from poisoning. Notably, solid-state NMR further proved that self-created tetrahedral coordination Al sites between MMT layers could accurately anchor poisoning cations in a targeted manner and protect the active centers. As shown in Figure 5, due to the self-created tetrahedrally coordinated Al sites between the MMT layers and pillared TiO<sub>2</sub> together anchoring the poisoning substances and thus protecting the active component CeO<sub>2</sub> from attacking, the active nitrate species could smoothly react with the adsorbed ammonia species. As for poisoned CeO<sub>2</sub>/TiO<sub>2</sub>, the poisoning cations influenced the active CeO<sub>2</sub> on the bulk TiO<sub>2</sub> support directly, thus severely blocking the reaction path. This work not only gives an effective antipoisoning strategy for designing smart NH<sub>3</sub>-SCR catalysts with excellent poisoning resistance

but also paves a new way for efficient reduction of NO<sub>x</sub> from the complex flue gas in practical applications.

## ■ ASSOCIATED CONTENT

### Supporting Information

The Supporting Information is available free of charge at <https://pubs.acs.org/doi/10.1021/acs.est.2c00758>.

Information about catalyst preparation; NO<sub>x</sub> reduction measurements; catalyst characterization; NO<sub>x</sub> conversion (Figures S1–S6); XRD patterns (Figures S7 and S8); SEM and SEM-EDS results (Figures S9–S13); TEM images, HRTEM images, and EDS line scan results (Figure S14); NH<sub>3</sub>-TPD-MS (Figure S15); pyridine-FTIR (Figure S16); H<sub>2</sub>-TPR (Figure S17); XPS spectra of Ce 3d (Figure S18); O 1s (Figures S20 and S21), Ti 2p (Figure S22), Si 2p (Figure S23), and Al 2p (Figure S24) of representative catalysts; surface K content analysis (Figure S19); solid-state NMR spectra (Figure S25); *in situ* DRIFTS (Figures S26–S33); weight content of elements (Table S1); specific surface area, pore volume, and pore size (Table S2); and total acid amount and acid loss ratio (Table S3) (PDF)

## ■ AUTHOR INFORMATION

### Corresponding Author

**Dengsong Zhang** – International Joint Laboratory of Catalytic Chemistry, College of Sciences, Shanghai University, Shanghai 200444, China; [orcid.org/0000-0003-4280-0068](https://orcid.org/0000-0003-4280-0068); Phone: +86-21-66134330; Email: [dszhang@shu.edu.cn](mailto:dszhang@shu.edu.cn)

### Authors

**Jialun Zhou** – International Joint Laboratory of Catalytic Chemistry, College of Sciences, Shanghai University, Shanghai 200444, China

**Penglu Wang** – International Joint Laboratory of Catalytic Chemistry, College of Sciences, Shanghai University, Shanghai 200444, China

**Aling Chen** – International Joint Laboratory of Catalytic Chemistry, College of Sciences, Shanghai University, Shanghai 200444, China



Wenqiang Qu – International Joint Laboratory of Catalytic Chemistry, College of Sciences, Shanghai University, Shanghai 200444, China

Yufei Zhao – International Joint Laboratory of Catalytic Chemistry, College of Sciences, Shanghai University, Shanghai 200444, China

Complete contact information is available at:

<https://pubs.acs.org/10.1021/acs.est.2c00758>

## Notes

The authors declare no competing financial interest.

## ACKNOWLEDGMENTS

We acknowledge the support of the National Natural Science Foundation of China (22125604 and 21976117).

## REFERENCES

- (1) Laughner, J. L.; Cohen, R. C. Direct observation of changing  $\text{NO}_x$  lifetime in North American cities. *Science* **2019**, *366*, 723–727.
- (2) Almaraz, M.; Bai, E.; Wang, C.; Trousdell, J.; Conley, S.; Faloon, I.; Houlton, B. Z. Agriculture is a major source of  $\text{NO}_x$  pollution in California. *Sci. Adv.* **2018**, *4*, No. 3477.
- (3) Inomata, Y.; Kubota, H.; Hata, S.; Kiyonaga, E.; Morita, K.; Yoshida, K.; Sakaguchi, N.; Toyao, T.; Shimizu, K. I.; Ishikawa, S.; Ueda, W.; Haruta, M.; Murayama, T. Bulk tungsten-substituted vanadium oxide for low-temperature  $\text{NO}_x$  removal in the presence of water. *Nat. Commun.* **2021**, *12*, No. 557.
- (4) Qu, W.; Liu, X.; Chen, J.; Dong, Y.; Tang, X.; Chen, Y. Single-atom catalysts reveal the dinuclear characteristic of active sites in NO selective reduction with  $\text{NH}_3$ . *Nat. Commun.* **2020**, *11*, No. 1532.
- (5) Jaegers, N. R.; Lai, J.; He, Y.; Walter, E.; Dixon, D. A.; Vasiliu, M.; Chen, Y.; Wang, C.; Hu, M.; Mueller, K. T.; Wachs, I. E.; Wang, Y.; Hu, J. Mechanism by which tungsten oxide promotes the activity of supported  $\text{V}_2\text{O}_5/\text{TiO}_2$  catalysts for  $\text{NO}_x$  abatement: Structural effects revealed by  $^{51}\text{V}$  MAS NMR spectroscopy. *Angew. Chem., Int. Ed.* **2019**, *58*, 12609–12616.
- (6) Xu, H.; Liu, J.; Zhang, Z.; Liu, S.; Lin, Q.; Wang, Y.; Dai, S.; Chen, Y. Design and synthesis of highly-dispersed  $\text{WO}_3$  catalyst with highly effective  $\text{NH}_3$ -SCR activity for  $\text{NO}_x$  abatement. *ACS Catal.* **2019**, *9*, 11557–11562.
- (7) Yan, L.; Wang, F.; Wang, P.; Impeng, S.; Liu, X.; Han, L.; Yan, T.; Zhang, D. Unraveling the unexpected offset effects of Cd and  $\text{SO}_2$  deactivation over  $\text{CeO}_2\text{-WO}_3/\text{TiO}_2$  catalysts for  $\text{NO}_x$  reduction. *Environ. Sci. Technol.* **2020**, *54*, 7697–7705.
- (8) Peng, Y.; Wang, D.; Li, B.; Wang, C.; Li, J.; Crittenden, J.; Hao, J. Impacts of Pb and  $\text{SO}_2$  poisoning on  $\text{CeO}_2\text{-WO}_3/\text{TiO}_2\text{-SiO}_2$  SCR catalyst. *Environ. Sci. Technol.* **2017**, *51*, 11943–11949.
- (9) Wang, B.; Wang, M.; Han, L.; Hou, Y.; Bao, W.; Zhang, C.; Feng, G.; Chang, L.; Huang, Z.; Wang, J. Improved activity and  $\text{SO}_2$  resistance by Sm-modulated redox of  $\text{MnCeSmTiO}_x$  mesoporous amorphous oxides for low-temperature  $\text{NH}_3$ -SCR of NO. *ACS Catal.* **2020**, *10*, 9034–9045.
- (10) Li, X.; Li, X.; Zhu, T.; Peng, Y.; Li, J.; Hao, J. Extraordinary deactivation offset effect of arsenic and calcium on  $\text{CeO}_2\text{-WO}_3$  SCR catalysts. *Environ. Sci. Technol.* **2018**, *52*, 8578–8587.
- (11) Peng, Y.; Li, J.; Shi, W.; Xu, J.; Hao, J. Design strategies for development of SCR catalyst: Improvement of alkali poisoning resistance and novel regeneration method. *Environ. Sci. Technol.* **2012**, *46*, 12623–12629.
- (12) Song, L.; Yue, H.; Ma, K.; Liu, W.; Tian, W.; Liu, C.; Tang, S.; Liang, B. FeSTi superacid catalyst for  $\text{NH}_3$ -SCR with superior resistance to metal poisons in flue gas. *ACS Sustainable Chem. Eng.* **2020**, *8*, 16878–16888.
- (13) Hu, W.; Zhang, Y.; Liu, S.; Zheng, C.; Gao, X.; Nova, I.; Tronconi, E. Improvement in activity and alkali resistance of a novel V-Ce( $\text{SO}_4$ ) $_2$ /Ti catalyst for selective catalytic reduction of NO with  $\text{NH}_3$ . *Appl. Catal., B* **2017**, *206*, 449–460.
- (14) Cai, S.; Xu, T.; Wang, P.; Han, L.; Impeng, S.; Li, Y.; Yan, T.; Chen, G.; Shi, L.; Zhang, D. Self-protected  $\text{CeO}_2\text{-SnO}_2@ \text{SO}_4^{2-}/\text{TiO}_2$  catalysts with extraordinary resistance to alkali and heavy metals for  $\text{NO}_x$  reduction. *Environ. Sci. Technol.* **2020**, *54*, 12752–12760.
- (15) Han, L.; Cai, S.; Gao, M.; Hasegawa, J. Y.; Wang, P.; Zhang, J.; Shi, L.; Zhang, D. Selective catalytic reduction of  $\text{NO}_x$  with  $\text{NH}_3$  by using novel catalysts: State of the art and future prospects. *Chem. Rev.* **2019**, *119*, 10916–10976.
- (16) Zhou, G.; Maitarad, P.; Wang, P.; Han, L.; Yan, T.; Li, H.; Zhang, J.; Shi, L.; Zhang, D. Alkali-resistant  $\text{NO}_x$  reduction over SCR catalysts via boosting  $\text{NH}_3$  adsorption rates by in situ constructing the sacrificed sites. *Environ. Sci. Technol.* **2020**, *54*, 13314–13321.
- (17) Zhang, J.; Huang, Z.; Du, Y.; Wu, X.; Shen, H.; Jing, G. Alkali-poisoning-resistant  $\text{Fe}_2\text{O}_3/\text{MoO}_3/\text{TiO}_2$  catalyst for the selective reduction of NO by  $\text{NH}_3$ : The role of the  $\text{MoO}_3$  safety buffer in protecting surface active sites. *Environ. Sci. Technol.* **2020**, *54*, 595–603.
- (18) Wang, P.; Chen, S.; Gao, S.; Zhang, J.; Wang, H.; Wu, Z. Niobium oxide confined by ceria nanotubes as a novel SCR catalyst with excellent resistance to potassium, phosphorus, and lead. *Appl. Catal., B* **2018**, *231*, 299–309.
- (19) Kéri, A.; Dahn, R.; Krack, M.; Churakov, S. V. Combined XAFS spectroscopy and Ab initio study on the characterization of iron incorporation by montmorillonite. *Environ. Sci. Technol.* **2017**, *51*, 10585–10594.
- (20) Qin, C.; Zhang, W.; Yang, B.; Chen, X.; Xia, K.; Gao, Y. DNA facilitates the sorption of polycyclic aromatic hydrocarbons on montmorillonites. *Environ. Sci. Technol.* **2018**, *52*, 2694–2703.
- (21) Peng, A.; Gao, J.; Chen, Z.; Wang, Y.; Li, H.; Ma, L.; Gu, C. Interactions of gaseous 2-chlorophenol with  $\text{Fe}^{3+}$ -saturated montmorillonite and their toxicity to human lung cells. *Environ. Sci. Technol.* **2018**, *52*, 5208–5217.
- (22) Xu, D.; Wu, W.; Wang, P.; Deng, J.; Yan, T.; Zhang, D. Boosting the alkali/heavy metal poisoning resistance for NO removal by using iron-titanium pillared montmorillonite catalysts. *J. Hazard. Mater.* **2020**, *399*, No. 122947.
- (23) Han, Z.; Yu, Q.; Xie, H.; Liu, K.; Qin, Q.; Xue, Z. Fabrication of manganese-based Zr-Fe polymeric pillared interlayered montmorillonite for low-temperature selective catalytic reduction of  $\text{NO}_x$  by  $\text{NH}_3$  in the metallurgical sintering flue gas. *Environ. Sci. Pollut. Res.* **2018**, *25*, 32122–32129.
- (24) Chen, D.; Feng, J.; Sun, J.; Cen, C.; Tian, S.; Yang, J.; Xiong, Y. Molybdenum modified montmorillonite clay as an efficient catalyst for low temperature  $\text{NH}_3$ -SCR. *J. Chem. Technol. Biotechnol.* **2020**, *95*, 1441–1452.
- (25) Yuan, M.; Deng, W.; Dong, S.; Li, Q.; Zhao, B.; Su, Y. Montmorillonite based porous clay heterostructures modified with Fe as catalysts for selective catalytic reduction of NO with propylene. *Chem. Eng. J.* **2018**, *353*, 839–848.
- (26) Dincer, B. Y.; Balci, S.; Tomul, F. In-situ mesoporous silica pillared clay synthesis and effect of titanium and iron incorporation to structural properties. *Microporous Mesoporous Mater.* **2020**, *305*, No. 110342.
- (27) Zhao, B.; Cheng, Z.; Zheng, J.; Wang, Z.; Zuo, S. Synthesis of  $\text{C}_{21}\text{H}_{38}\text{ClN}$  assisted Si pillared clays and the effects of  $\text{CeO}_2$  addition on its supported palladium catalyst for benzene oxidation. *Catal. Lett.* **2021**, *151*, 3287–3297.
- (28) Zhao, Y.; Shi, L.; Shen, Y.; Zhou, J.; Jia, Z.; Yan, T.; Wang, P.; Zhang, D. Self-defense effects of Ti-modified attapulgite for alkali-resistant  $\text{NO}_x$  catalytic reduction. *Environ. Sci. Technol.* **2022**, *56*, 4386–4395.
- (29) Li, Y.; Cai, S.; Wang, P.; Yan, T.; Zhang, J.; Zhang, D. Improved  $\text{NO}_x$  reduction over phosphate-modified  $\text{Fe}_2\text{O}_3/\text{TiO}_2$  catalysts via tailoring reaction paths by in situ creating alkali-poisoning sites. *Environ. Sci. Technol.* **2021**, *55*, 9276–9284.
- (30) Sun, P.; Wang, W.; Weng, X.; Dai, X.; Wu, Z. Alkali potassium induced HCl/ $\text{CO}_2$  selectivity enhancement and chlorination reaction inhibition for catalytic oxidation of chloroaromatics. *Environ. Sci. Technol.* **2018**, *52*, 6438–6447.

- (31) Yan, Q.; Chen, S.; Zhang, C.; Wang, Q.; Louis, B. Synthesis and catalytic performance of  $\text{Cu}_1\text{Mn}_{0.5}\text{Ti}_{0.5}\text{O}$  mixed oxide as low-temperature  $\text{NH}_3$ -SCR catalyst with enhanced  $\text{SO}_2$  resistance. *Appl. Catal., B* **2018**, 238, 236–247.
- (32) Liu, F.; Wang, T.; Zheng, Y.; Wang, J. Synergistic effect of Brønsted and Lewis acid sites for the synthesis of polyoxymethylene dimethyl ethers over highly efficient  $\text{SO}_4^{2-}/\text{TiO}_2$  catalysts. *J. Catal.* **2017**, 355, 17–25.
- (33) Fei, Z.; Yang, Y.; Wang, M.; Tao, Z.; Liu, Q.; Chen, X.; Cui, M.; Zhang, Z.; Tang, J.; Qiao, X. Precisely fabricating Ce-O-Ti structure to enhance performance of Ce-Ti based catalysts for selective catalytic reduction of NO with  $\text{NH}_3$ . *Chem. Eng. J.* **2018**, 353, 930–939.
- (34) Zhang, L.; Li, L.; Cao, Y.; Xiong, Y.; Wu, S.; Sun, J.; Tang, C.; Gao, F.; Dong, L. Promotional effect of doping  $\text{SnO}_2$  into  $\text{TiO}_2$  over a  $\text{CeO}_2/\text{TiO}_2$  catalyst for selective catalytic reduction of NO by  $\text{NH}_3$ . *Catal. Sci. Technol.* **2015**, 5, 2188–2196.
- (35) Kang, L.; Han, L.; He, J.; Li, H.; Yan, T.; Chen, G.; Zhang, J.; Shi, L.; Zhang, D. Improved  $\text{NO}_x$  reduction in the presence of  $\text{SO}_2$  by using  $\text{Fe}_2\text{O}_3$ -promoted halloysite-supported  $\text{CeO}_2\text{-WO}_3$  catalysts. *Environ. Sci. Technol.* **2019**, 53, 938–945.
- (36) Wang, Q.; Li, Y.; Serrano-Lotina, A.; Han, W.; Portela, R.; Wang, R.; Banares, M. A.; Yeung, K. L. Operando investigation of toluene oxidation over 1D  $\text{Pt@CeO}_2$  derived from Pt cluster-containing MOF. *J. Am. Chem. Soc.* **2021**, 143, 196–205.
- (37) Nong, S.; Dong, W.; Yin, J.; Dong, B.; Lu, Y.; Yuan, X.; Wang, X.; Bu, K.; Chen, M.; Jiang, S.; Liu, L.; Sui, M.; Huang, F. Well-dispersed ruthenium in mesoporous crystal  $\text{TiO}_2$  as an advanced electrocatalyst for hydrogen evolution reaction. *J. Am. Chem. Soc.* **2018**, 140, 5719–5727.
- (38) Zhao, W.; Zhang, K.; Wu, L.; Wang, Q.; Shang, D.; Zhong, Q.  $\text{Ti}^{3+}$  doped  $\text{V}_2\text{O}_5/\text{TiO}_2$  catalyst for efficient selective catalytic reduction of  $\text{NO}_x$  with  $\text{NH}_3$ . *J. Colloid Interface Sci.* **2021**, 581, 76–83.
- (39) Lelli, M.; Gajan, D.; Lesage, A.; Caporini, M. A.; Vitzthum, V.; Mieville, P.; Heroguel, F.; Rascon, F.; Roussey, A.; Thieuleux, C.; Boualleg, M.; Veyre, L.; Bodenhausen, G.; Coperet, C.; Emsley, L. Fast characterization of functionalized silica materials by silicon-29 surface-enhanced NMR spectroscopy using dynamic nuclear polarization. *J. Am. Chem. Soc.* **2011**, 133, 2104–2107.
- (40) Gore, K. U.; Abraham, A.; Hegde, S. G.; Kumar, R.; Amoureux, J. P.; Ganapathy, S. Si-29 and Al-27 MAS/3Q-MAS NMR studies of high silica USY zeolites. *J. Phys. Chem. B* **2002**, 106, 6115–6120.
- (41) Yan, L.; Ji, Y.; Wang, P.; Feng, C.; Han, L.; Li, H.; Yan, T.; Shi, L.; Zhang, D. Alkali and phosphorus resistant zeolite-like catalysts for  $\text{NO}_x$  reduction by  $\text{NH}_3$ . *Environ. Sci. Technol.* **2020**, 54, 9132–9141.
- (42) Fan, J.; Ning, P.; Song, Z.; Liu, X.; Wang, L.; Wang, J.; Wang, H.; Long, K.; Zhang, Q. Mechanistic aspects of  $\text{NH}_3$ -SCR reaction over  $\text{CeO}_2/\text{TiO}_2\text{-ZrO}_2\text{-SO}_4^{2-}$  catalyst: In situ DRIFTS investigation. *Chem. Eng. J.* **2018**, 334, 855–863.
- (43) Wei, L.; Cui, S.; Guo, H.; Zhang, L. The effect of alkali metal over  $\text{Mn}/\text{TiO}_2$  for low-temperature SCR of NO with  $\text{NH}_3$  through DRIFT and DFT. *Comput. Mater. Sci.* **2018**, 144, 216–222.
- (44) Wang, K.; Gong, Z.; Luo, H.; Jin, K.; Hua, Y.; Wu, W. DRIFT study of the adsorption of  $\text{NH}_3$  and  $\text{NO}_x$  over rare earth concentrate enriched from bayan obo tailings. *Combust. Sci. Technol.* **2018**, 190, 770–783.
- (45) Liu, Z.; Liu, H.; Feng, X.; Ma, L.; Cao, X.; Wang, B. Ni-Ce-Ti as a superior catalyst for the selective catalytic reduction of  $\text{NO}_x$  with  $\text{NH}_3$ . *Mol. Catal.* **2018**, 445, 179–186.
- (46) Hu, H.; Cai, S.; Li, H.; Huang, L.; Shi, L.; Zhang, D. In situ DRIFTS investigation of the low-temperature reaction mechanism over Mn-doped  $\text{Co}_3\text{O}_4$  for the selective catalytic reduction of  $\text{NO}_x$  with  $\text{NH}_3$ . *J. Phys. Chem. C* **2015**, 119, 22924–22933.
- (47) Weng, X.; Dai, X.; Zeng, Q.; Liu, Y.; Wu, Z. DRIFT studies on promotion mechanism of  $\text{H}_3\text{PW}_{12}\text{O}_{40}$  in selective catalytic reduction of NO with  $\text{NH}_3$ . *J. Colloid Interface Sci.* **2016**, 461, 9–14.
- (48) Liu, N.; Wang, J.; Wang, F.; Liu, J. Promoting effect of tantalum and antimony additives on de $\text{NO}_x$  performance of  $\text{Ce}_3\text{Ta}_3\text{SbO}_x$  for  $\text{NH}_3$ -SCR reaction and DRIFT studies. *J. Rare Earths* **2018**, 36, 594–602.
- (49) Zhang, Q.; Fan, J.; Ning, P.; Song, Z.; Liu, X.; Wang, L.; Wang, J.; Wang, H.; Long, K. In situ DRIFTS investigation of  $\text{NH}_3$ -SCR reaction over  $\text{CeO}_2/\text{zirconium phosphate}$  catalyst. *Appl. Surf. Sci.* **2018**, 435, 1037–1045.
- (50) Liu, K.; Liu, F.; Xie, L.; Shan, W.; He, H. DRIFTS study of a Ce-W mixed oxide catalyst for the selective catalytic reduction of  $\text{NO}_x$  with  $\text{NH}_3$ . *Catal. Sci. Technol.* **2015**, 5, 2290–2299.
- (51) Chen, Y.; Wang, J.; Yan, Z.; Liu, L.; Zhang, Z.; Wang, X. Promoting effect of Nd on the reduction of NO with  $\text{NH}_3$  over  $\text{CeO}_2$  supported by activated semi-coke: An in situ DRIFTS study. *Catal. Sci. Technol.* **2015**, 5, 2251–2259.

## Recommended by ACS

### Targeted NO Oxidation and Synchronous $\text{NO}_2$ Inhibition via Oriented $\text{O}_2$ Formation Based on Lewis Acid Site Adjustment

Songxia Wang, Fan Dong, *et al.*

AUGUST 17, 2023

ENVIRONMENTAL SCIENCE & TECHNOLOGY

READ 

### Facile $\text{H}_2\text{O}$ -Contributed $\text{O}_2$ Activation Strategy over Mn-Based SCR Catalysts to Counteract $\text{SO}_2$ Poisoning

Dongqi An, Lin Dong, *et al.*

SEPTEMBER 22, 2023

ENVIRONMENTAL SCIENCE & TECHNOLOGY

READ 

### Site-Selective Nitrogen-Doped $\alpha\text{-MnO}_2$ for Catalytic Oxidation of Carcinogenic HCHO in Indoor Air

Taohong He, Shaopeng Rong, *et al.*

JUNE 14, 2022

ACS ES&T ENGINEERING

READ 

### Selective $\text{NO}_x$ -Electroreduction to Ammonia on Isolated Ru Sites

Zunjian Ke, Xiangheng Xiao, *et al.*

FEBRUARY 06, 2023

ACS NANO

READ 

Get More Suggestions >